Flow of Foams

Katgert, G.

Chapter 4

Packing fraction and Jamming

The experiments described in Chapters 2 and 3 have been performed at a fixed gap between the liquid surface and the glass plate. However, by increasing or decreasing this gap we can vary the packing density of the foam [61, 92]. While the precise relation between the gap and the packing density is nontrivial we can understand the main trend as follows: it is energetically favorable for the bubbles to contact both the glass top plate and the fluid phase. Hence, increasing the gap stretches the bubbles vertically, and more bubbles can be packed per unit area. The change in bubble shape is such that the size of the contacts between bubbles increases, and the liquid fraction in horizontal cross sections decreases — effectively, the liquid fraction goes down, and seen from above, the foam looks 'dry'. Similarly, decreasing the gap leads to pancake shaped, circular bubbles [18] and the foam becomes 'wet'. Clearly, there are limits to the range of available liquid fractions, as the bubbles form multilayers as the gap is increased too much.

As we will explain below, we will quantify the wetness of the foam by an effective packing fraction ϕ, which essentially can be thought of as the 2D packing fraction of the gas bubbles seen in the midplane between fluid surface and top plate. Hence, the dry limit corresponds to $\phi \approx 1$, while the wet limit corresponds to $\phi \approx 0.84$ [23, 33, 93]. In practice, our data is limited to the range $0.855 \lesssim \phi \lesssim 0.975$.

In this chapter, in section 4.1, we first establish how to extract the packing fraction ϕ from the experimental images, and also define an algorithm that determines whether neighboring bubbles are in contact or not. We

then compare the scaling of the contact number Z with packing fraction ϕ, and find, for the first time for a system of frictionless deformable spherical entities, that our data agrees well with the square-root scaling established in the seminal papers of Durian [23] and O'Hern et al. [6].

In section 4.2, we probe the role of the packing density for the flow of foams in the linear shear cell. Clearly, varying the gap, which implies stretching the bubbles, varying their contact area and varying ϕ, should have a significant impact on the shape of the velocity profile, since the size of the deformed facets between neighboring bubbles influences the magnitude of their drag forces. By varying the driving rate in the shear cell for a range of packing fractions, we establish that the exponent governing the averaged bubble-bubble drag forces (β) is independent of ϕ, while the proportionality factor k, which measures the ratio of the pre-factors f_{bb} and f_{bw}, see chapter 2, varies strongly with liquid fraction. We will argue that the main variation in k will be due to variations of the bubble-bubble interactions, characterized by f_{bb}.

In section 4.3, we explore the use of our foam to study aspects of scaling near the jamming transition of frictionless deformable spherical entities. We first study the distribution of free area per bubble by means of a Voronoi area distribution in our foam, we then estimate the inter-bubble contact force distributions and finally present preliminary measurements on the variation of the static shear modulus G with packing fraction ϕ.

4.1 Varying and measuring ϕ

In order to vary ϕ, we vary the gap width between the glass plate and the bulk solution between 3 and 0.2 mm. We do this by adding or retracting fluid from the reservoir. To have a homogeneous gap between the liquid surface and the glass plate, we place additional supports under the glass plate to prevent sagging of the top plate during the runs. We monitor the gap width with a Mitutoyo digital depth gauge. If the gap becomes smaller than 0.2 mm the bubbles unjam [92]. This might be due to the fact that the gap is then of the size of the Plateau borders that connect the flat film between the bubble and the glass plate and the flat film between neighbouring bubbles, and hence the latter vanishes. If the gap becomes larger than 3 mm the foam buckles and develops a three dimensional structure.

If we stay between these limits the system we study is jammed and

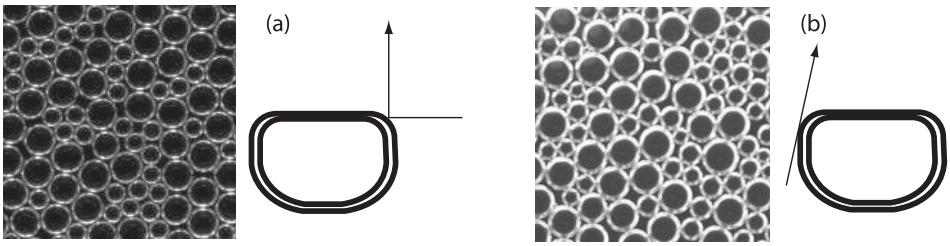

FIGURE 4.1: (a). Images as used in chapter 2 and 3: lateral lighting reflects off the Plateau border and which bubbles do actually touch is unclear. (b) Images obtained by lighting slanted from below. Contacts are now clearly visible.

quasi two-dimensional. However, determining a liquid fraction is not trivial, since various horizontal cuts through the bubble layer will yield different values. Various measures can be employed. First of all, one could try to relate the liquid fraction to the gap between the liquid surface and the glass plate. This distance, however, does not unambiguously set ϕ in our experiment: we observe a large hysteresis effect, i.e., increasing or decreasing the gap to a certain value does not yield the same packing fraction ϕ. We speculate this is due to the fact that the bubbles are not confined in the lateral direction i.e., the bubbles are not contained by side-walls. As a result, ϕ actually depends on both the gap distance and an ill defined confining pressure, which itself may be history dependent.

Another measure that has been derived in [61] relates the measured length of the deformed facets of the bubbles just before a T1 event to ϕ. In our experiments, though, we have found no well defined cut-off for such T1-events. It is not clear how the occurrence of T1-events can precisely be defined, since there is no obvious separation of the deformation scales during and outside of a T1-event.

4.1.1 Direct measure of ϕ from experimental images

In view of the difficulties outlined above, we measure ϕ by direct imaging as the two dimensional area fraction that is occupied by bubbles in our system. The lighting is crucial here, since clearly we image a highly nonlinear medium, and the observed bubble shape is a complex function of its true three dimensional shape. In the previous chapters, the bubbles were lit laterally. As a result, light was reflected towards the camera at the

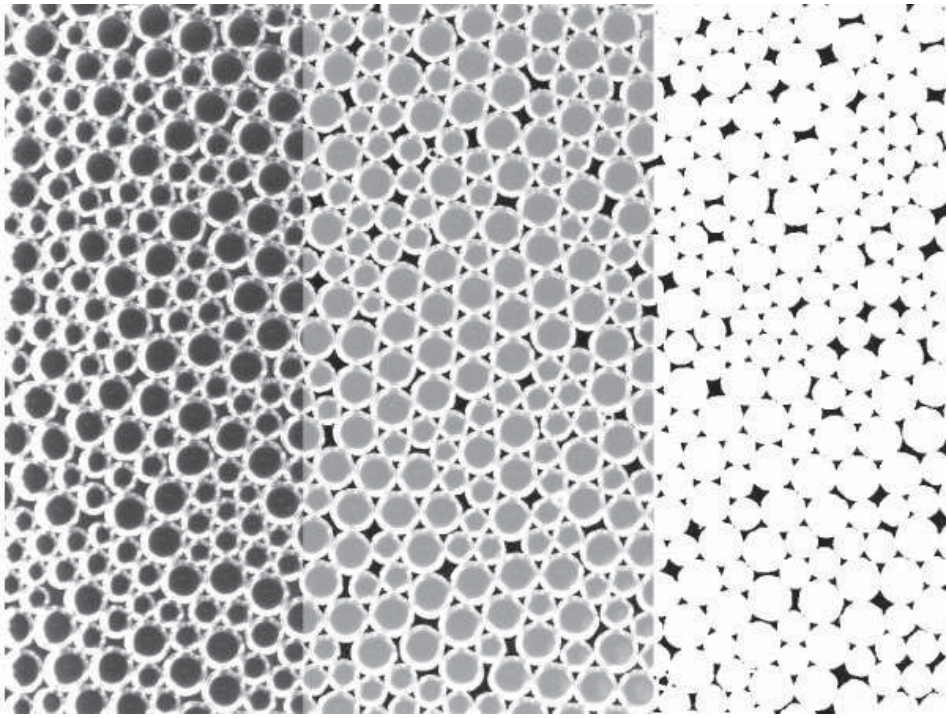

FIGURE 4.2: From left to right (1) Raw image. (2) Raw image with bubble areas superposed. Note the good agreement. (3) Only bubble areas in white.

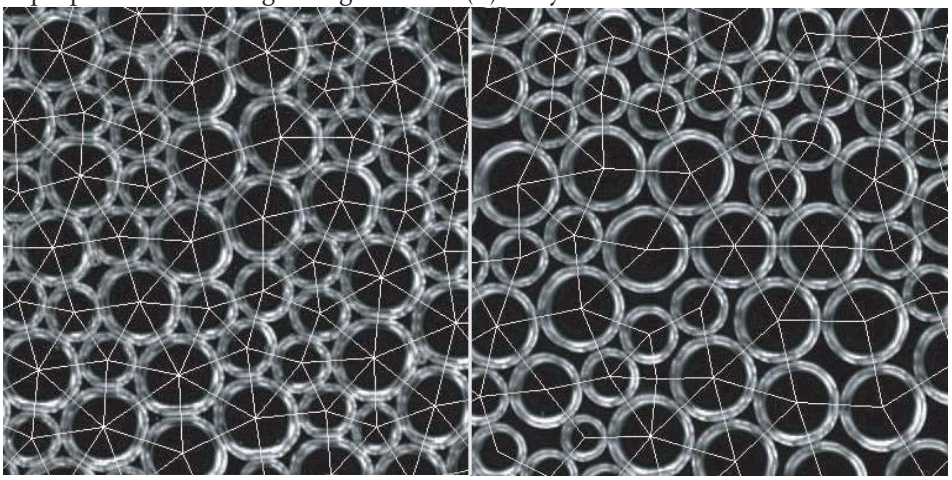

FIGURE 4.3: left-hand image: contacts as determined from Delaunay triangulation for a dry foam $\phi = 0.965$, right-hand image: contacts as determined for a wet foam, $\phi = 0.875$.

point were the Plateau border was under an angle of $45°$ with the vertical, see Fig. 4.1(a), resulting in rings that are smaller than the maximum lateral bubble cross-section. By switching to lighting the bubbles slanted from below we can visualise the full bubble diameter, see Fig. 4.1(b).

The procedure to extract ϕ from the images is illustrated in Fig. 4.2. We first binarise the images, after which both the bubble centers and the interstices appear bright. We remove the interstices by morphological operations. We then invert the binarised image and fill up the remaining bubble contours with a dilated version of the bubble centers. We check that the resulting bright disc optimally matches the original bubble contour, see Fig. 4.2. We then calculate the ratio of white pixels over the total number of pixels and hence obtain a reasonable estimate of ϕ.

We find that in the linear shear cell the accessible range in ϕ is $0.86 \lesssim \phi \lesssim 0.97$. It should be noted that for the runs performed at fixed wetness, discussed in the previous chapters, we find $\phi = 0.965 \pm 0.005$, in reasonable agreement with previous reports on the maximum ϕ that can be obtained in our type of setup [61].

4.1.2 The contact number Z and its scaling with ϕ

We can perform a consistency check on our measurements of ϕ by looking at the corresponding averaged number of contacts per bubble Z. By comparing to theoretical results, we can check whether the measured values of Z and ϕ correlate as expected and hence we have another indication of ϕ.

We extract Z from the images as follows. Starting from experimental images such as Fig. 4.3(a), we first locate the center of mass of the bubbles. We then perform a Delaunay triangulation on the resulting grid of points. All grid points are thus connected to all their nearest neighbours. However, not all neighbours are actually in contact. To remove the false contacts we measure the pixel intensity in the corresponding "ϕ-plot", see Fig. 4.2(c), along the vectors connecting any two bubbles, see Fig. 4.4. We then count the number of contacting bubbles for bubble and calculate the average over a large number of bubbles and images. Examples for a wet and a dry foam are depicted in Fig. 4.3: the left picture is of a dry foam, for which the gap between the glass plate and the liquid is large, the bubbles are strongly deformed and stretched, while the right picture is of a wet foam, for which the gap between liquid and glass plate is small, the bub-

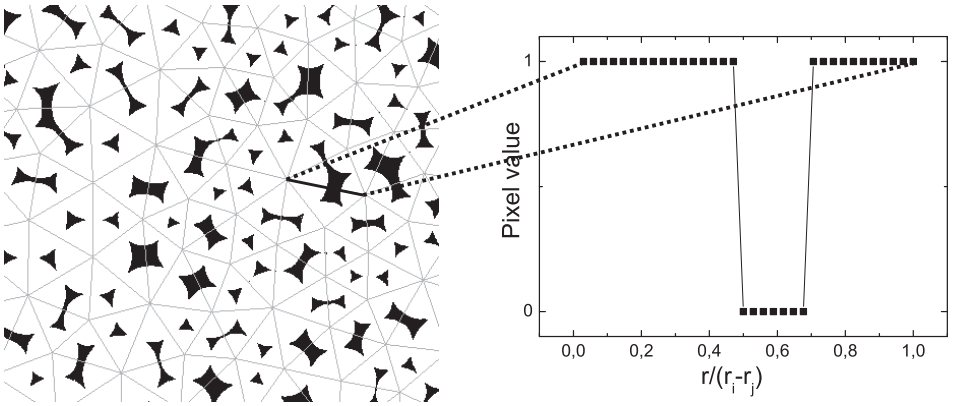

FIGURE 4.4: Plot of graph used to extract ϕ with Delaunay triangulation overplotted. To calculate Z, vectors that connect two bubbles that do not touch are removed by looking for a dip in the pixel intensity along the vector.

bles barely touch and are marginally stretched in the vertical direction.

We have checked whether the measurements of ϕ and Z are consistent by comparing these to prior theoretical predictions of the scaling behavior of Z with ϕ. Simulations of frictionless two-dimensional systems [6, 23] show that Z tends to $Z_c = 4$ if ϕ approaches $\phi_c = 0.842$ at the jamming point J. Away from this critical point these authors find:

$$Z - Z_c = Z_0 \left(\phi - \phi_c\right)^{1/2}. \tag{4.1}$$

This implies that if we know Z we can infer the packing fraction ϕ. We can also directly obtain a value of Z_0 since for very compressed foams ($\phi \to 1, \Delta\phi \equiv \phi - \phi_c \to 0.158$), Z approaches 6. This gives us $Z_0 = 5.06$. Note that in the numerical simulations of O'Hern et al. $Z_0 = 3$ [6].

We extract both ϕ and Z from the following experimental runs. We shear a bidisperse monolayer of foam in the linear geometry from chapter 2 at a fixed driving velocity $v_0 = 0.26$ mm/s. We perform a scan in ϕ for a gap width W of 5 cm and a scan in ϕ for a gap width of 7 cm. We obtain 3000 images per packing fraction, and to obtain statistically independent packings, we only analyze every 100th image, thus averaging both ϕ and z over 30 images, each containing approximately 500 bubbles.

The result is plotted in Fig. 4.5: for both widths the data points follow the same trend and if we overplot the numerical prediction from Eq. (4.1)

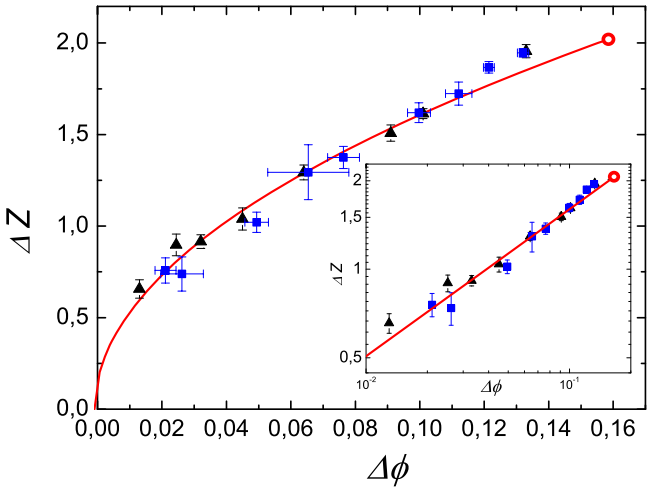

FIGURE 4.5: $Z - Z_c$ as a function of $\phi - \phi_c$, both averaged over 60 frames for a 5 cm gap (triangles) and a 7 cm gap (squares). Solid red line: $Z - Z_c = Z_0(\phi - \phi_c)^{0.5}$ with $Z_0 = 5.06$. Inset shows same plot on log-log scale. Open circle shows value used to calculate Z_0.

with $\phi_c = 0.842$ and $Z_0 = 5.06$ we obtain a reasonable match with the experimental datapoints. Note that we are not the first to have performed such an analysis. In fact Majmudar et al. [94] found the same scaling to hold in a frictional granular but their comparison to frictionless disc simulations seems inappropriate, whereas in our case the comparison is entirely valid. Moreover, the value of Z_0 the authors find in order to fit the data is anomalously high.

4.2 Scaling of the effective viscosity with ϕ

4.2.1 ϕ-dependence of β

Now that we can obtain good estimates of the packing fraction ϕ, we are in a position to investigate the variation of the flow behavior with ϕ, and in particular the functional dependence of the proportionality constant k on ϕ. In chapter 2 our drag force balance model yielded a k that sets the relative influence of the bubble-wall drag with respect to the bubble-

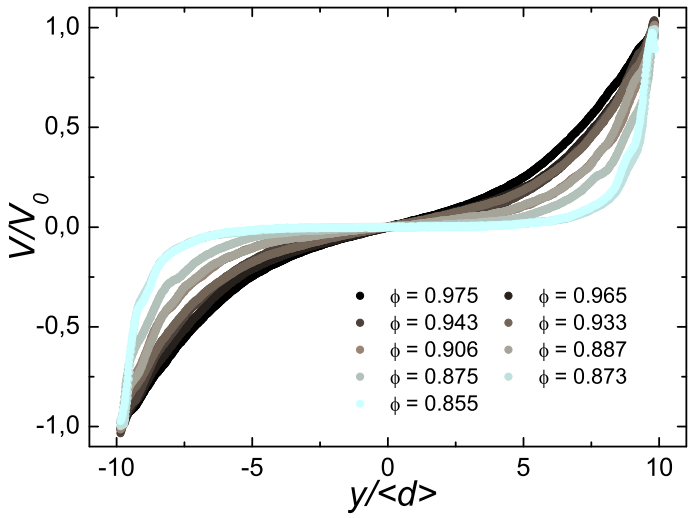

FIGURE 4.6: Velocity profiles from runs performed at a gap width $W = 5$ cm. For all runs, $v_0 = 0.26$ mm/s. Note that some profiles overlap and are thus hidden from view. The closer the density approaches the jamming point, the more shearbanded the velocity profiles become.

bubble drag and is given by $k \propto r_c/\kappa_c$ with r_c the radius of the flattened contact between the bubble and the wall and κ_c the radius of the flattened contact between neighbouring bubbles. Note that actual relation might well read $k \propto r_c^n/\kappa_c^m$, with n, m power law indices, but in principe the functional dependence of k on the two radii should assume a similar ratio.

While r_c is set by the buoyancy and hence does not vary strongly with the gap distance between glass plate and liquid surface — only becoming slightly smaller as the bubbles get stretched at large gaps — κ_c is strongly dependent on the gap size and hence on the packing fraction of the foam. We thus speculate that k will decrease with increasing ϕ as the size of the deformed facets between bubbles increases.

In order to extract k as a function of ϕ we extract averaged velocity profiles from runs at different wetness and fixed driving velocity. In Fig. 4.6 we plot velocity profiles obtained for a gap width $W = 5$ cm at a driving velocity $v_0 = 0.26$ mm/s and $0.855 \leq \phi \leq 0.975$. As ϕ is lowered, the profiles become more and more shearbanded, as expected.

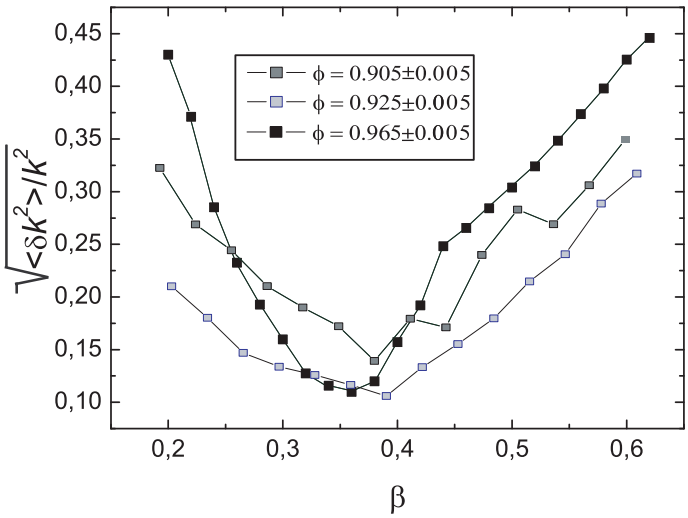

FIGURE 4.7: (a) variance in k values for all six runs performed at $\phi = 0.905$ (grey squares) and $\phi = 0.925$ (light grey squares). The variance at $\phi = 0.965$ (black squares) is data from Fig. 2.9(f). A clear minimum can be observed around $\beta = 0.38$.

We would like to fit solutions of the linear drag force balance model defined in Eq. (2.8) while keeping α and β fixed. The microscopic exponent α which governs the flow a bubble past a wall appears to be independent of the particularities of the foam flow (see section 2.4 and [95, 96]). On the other hand, it is not at all obvious that β, which governs the averaged bubble-bubble drag forces, does not depend on ϕ. As we have seen in chapter 2, β is set by the disorder in the system and the non-affine bubble motion that occurs in conjunction with that. Simulations [80] have shown that this non-affine behaviour strongly depends on ϕ, and therefore the averaged viscous drag could scale differently between different liquid fractions.

To see if this indeed occurs we perform a scan over the same six shear rates as employed in chapter 2 for a bidisperse foam at a gap width $W = 7$ cm, while first fixing $\phi = 0.905 \pm 0.005$ and then $\phi = 0.925 \pm 0.005$. We look for a minimum of the variance in k over the six velocity profiles as a function of β (see green and blue squares in Fig. 4.7). We subsequently fix this β and observe that the model fits best to all six runs performed at

$\phi = 0.905$ for $\alpha = 2/3, \beta = 0.38 \pm 0.05$ (see Fig. 4.7) and $k = 7.5$, whereas the model best matches the runs performed at $\phi = 0.925$ for $\alpha = 2/3, \beta = 0.39 \pm 0.05$ (see Fig. 4.7) and $k = 5.8$, thus strongly indicating that within our range of accessible liquid fractions β seems to be a constant while k varies. For comparison, we include the variance for the runs described in chapter 2, that were plotted in Fig. 2.9(f).

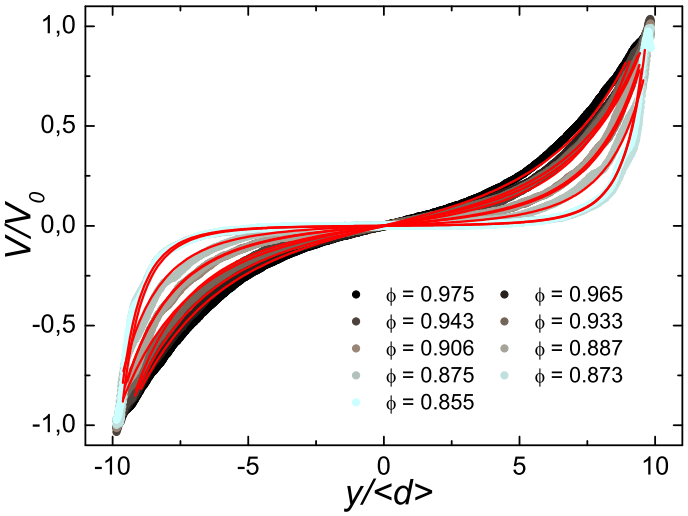

FIGURE 4.8: Velocity profiles from Fig. 4.6. Fits are solutions to linear drag force balance model with $\alpha = 0.67$ and $\beta = 0.36$ fixed. k is extracted from the fits and plotted in Fig. 4.9 as a function of $\phi - \phi_c$.

4.2.2 Scaling of k with ϕ

We measure velocity profiles at gap widths $W = 5$ cm, see Fig. 4.6, and $W = 7$ cm and fixed $v_0 = 0.26$ mm/s (the 3$^{\text{rd}}$ slowest driving velocity), for liquid fractions varying between $\phi = 0.855$ and $\phi = 0.975$. To these profiles we fit solutions of our drag force balance model with $\alpha = 0.67$ and $\beta = 0.36$ fixed while varying k, see Fig. 4.8. The best fit yields k and we plot it as a function of $\phi - \phi_c$, with ϕ_c the theoretically predicted and experimentally measured value of the unjamming packing fraction: $\phi_c = 0.842$ [33, 93, 97]. The result can be seen in Fig. 4.9.

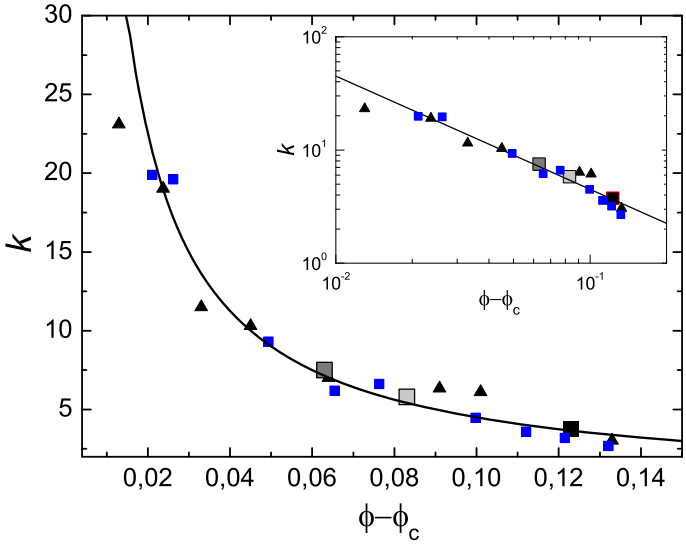

FIGURE 4.9: (b) Scaling of k with $\Delta\phi \equiv \phi - \phi_c$. Triangles: data obtained from fits depicted in Fig. 4.8 where W = 5 cm. Squares: data for gap of 7 cm. Large squares correspond to runs at v_0 =0.26 mm/s from Fig. 4.7. Solid line: $0.45/\Delta\phi$. Inset: same data on log-log scale.

The large squares represent the k-value extracted from the strain rate sweeps detailed in Fig. 4.7. The blue squares represent k-values found by fitting the model to the runs performed at a gap of 7 cm, whereas the black triangles are from the 5 cm gap run. We remind the reader that these runs have also provided the $\Delta Z(\Delta\phi)$-scaling in Fig. 4.5 where the color coding is the same.

In Fig. 4.8 we observe increasingly shearbanded velocity profiles as we approach ϕ_c. This trend is reflected in the increase of k as we approach ϕ_c. This implies that the deformed contact radius κ_c between bubbles becomes smaller and smaller. Note that this trend is opposite to what was observed by Debrégeas et al. in [9]: there the authors find that the velocity profiles become less shearbanded with increasing liquid fraction (see inset of Fig. 2.2). We cannot explain this result and conclude it to be one of the many mysteries surrounding that work.

As a guide to the eye we have plotted $k \propto \Delta\phi^{-1}$, and we will now try to relate the measured scaling of k with a simple argument for which we

need to include a prediction from recent work by Denkov et al. [25].

In chapter 1 we have discussed the relation between the dimensionless overlap $\delta\xi$ and the deformed contact κ_c. From Eq. (1.16) we recall that the size of κ_c should depend on the deformation $\delta\xi$ as:

$$\kappa_c \propto (\delta\xi)^{1/2}. \tag{4.2}$$

Furthermore, in simulations of two-dimensional frictionless discs [6, 80] it was found that

$$\delta\xi \propto \Delta\phi. \tag{4.3}$$

Assuming that r_c does not vary much with ϕ, simple substitution thus gives us

$$k \propto 1/(\Delta\phi)^{1/2}. \tag{4.4}$$

The scaling we measure does not agree with this simple prediction. The inset of Fig. 4.9 clearly shows the scaling of k with $\phi - \phi_c$ is steeper than expected from the simple calculation presented above. However, the assumption that the bubble-bubble drag scales linearly with κ_c has been shown to be false in a recent paper by Denkov an coworkers. In fact, the authors show that the viscous dissipation inside foams scales as κ_c^2 instead. Inserting this in the above equations yields:

$$k \propto 1/(\Delta\phi), \tag{4.5}$$

which is fully consistent with our experimental results.

Note that in the above we have only focussed on the radius of the deformed facets. A proper analysis would include the size of the Plateau border around the contact, which is where the dissipation also occurs [21, 22]. For instance, in [96] the bubble-wall drag force scales as $F^{bw} \propto Ca^{0.64}\phi_l^{-0.26}$ and a proper treatment would entail such analysis, even though the functional dependence on the Plateau border size is always weak. Moreover, the Plateau border size itself does not vary by large amounts in the region of ϕ we measure in. Moreover, in all of these works, the functional dependence of the drag force with ϕ is smooth around ϕ_c and hence will not influence the critical scaling at that point.

4.3 Measures of jamming: Voronoi area distribution, $p(f)$ and shear modulus

In 1998, Liu and Nagel [2] introduced the jamming phase diagram in an attempt to describe jamming in a wide variety of materials that, while having a wildly dissimilar appearance, share similar behaviour under, for instance, an applied force. Foams (shaving foam), pastes (peanut butter), emulsions (mayonnaise) and granulates (sugar) can all carry a finite load like a solid, but will flow like a liquid once enough stress is applied. All of these systems consist of elementary building blocks (grains, droplets, bubbles) that are closely packed and jammed at rest and have to overcome steric hindrance and hence deform elastically before they can flow, giving rise to the combination of solid-like and liquid like behaviour.

The jamming diagram has led to an upsurge of scientific interest and in a short time, much theoretical progress has been made - in particular, simulation studies on soft two-dimensional frictionless discs at zero stress, zero temperature and varying packing density ϕ, close to "Point J" (see Fig. 4.10), have yielded much insight [6, 80, 98]. "Point J" corresponds to a critical packing fraction ϕ_c where systems unjam because the density of particles becomes too low for the system to bear a finite load.

If someone familiar with this recent work on the jamming transition in the (Σ, ϕ)-plane were to glance through this thesis, he or she should have to conclude that disordered two-dimensional foams seem to be the ideal candidate to experimentally probe the proposed behaviour [6,80,93] around the jamming transition in frictionless systems. Foam bubbles obey a Hookean interaction law upon compression, do not exhibit solid friction upon sliding and, if appropriately confined by a glass plate, the packing fraction can be varied over a considerable range.

In order to substantiate this idea we will present some highly exploratory and preliminary data on a few measures that are connected to the jamming framework. We will first apply a particular Voronoi tessellation called the navigation map to our experimental images to extract the distribution of free area per bubble in the spirit of Aste et al. [99]. Then, with help from this navigation map, we extract the distribution of contact forces $p(f)$ in the foam and investigate its scaling with ϕ and we conclude with the first preliminary measurements of the scaling of the static shear modulus G with ϕ.

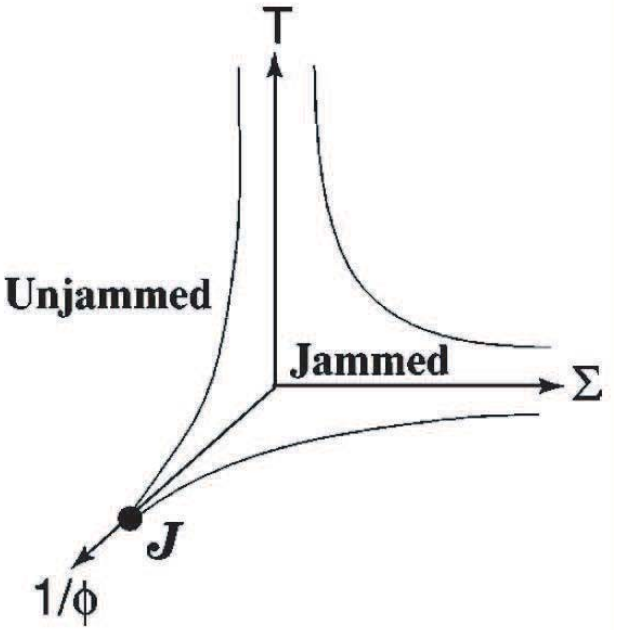

FIGURE 4.10: The jamming phase diagram as proposed in [6]: if the temperature T, the applied stress Σ and the inverse particle density $1/\phi$ are sufficiently small, the system is jammed. Note that all foam experiments are performed in the (Σ, ϕ)-plane.

4.3.1 Voronoi area distribution

Granular thermodynamics

The thermodynamical description of granular materials, as introduced by Edwards and Oakeshott [100] tries to translate the concepts underpinning equilibrium thermodynamics to conglomerates of a-thermal particles such as grains. To this end the granular entropy is introduced as

$$S = \ln \Omega(V), \tag{4.6}$$

with $\Omega(V)$ the number of microstates that can be classified under a coarse-grained volume V. Note that it is assumed that all states are equally accessible. In this framework, for granular systems the volume thus takes the

role of energy and the global volume V_T of the granular packing is given. The granular temperature β_{gr} is then, as in equilibrium thermodynamics, defined through

$$\beta_{gr} = \frac{\partial S}{\partial V}. \tag{4.7}$$

In thermal systems, $\beta = 1/k_B T$. In granular systems β is related in a similar way to a compactivity χ: $\beta_{gr} = 1/\chi$.

The granular analogue of the Maxwell-Boltzmann distibution that describes the distribution of free volumes V in a $p(V)$ can be found by searching for the functional form of the probability distribution function which maximizes the entropy. Such maximization must be done under the condition that the average occupied volume is equal to $\bar{V}$. This yields:

$$p(V) = \frac{\Omega(V) e^{V/\chi}}{\sum_{V'} \Omega(V') e^{V'/\chi}}. \tag{4.8}$$

Aste and Di Matteo [101] find an analytical expression for $\Omega(V)$ under the assumption that the system consists of elementary cells each weighted according to $p(v) = \frac{1}{\chi} e^{-(v - v_{min})/\chi}$ with the compactivity $\chi = \langle v \rangle - v_{min}$ an intensive thermodynamic parameter accounting for the exchange of volume between the elementary cell and the surrounding volume 'reservoir'. The elementary space partitions that can be measured, such as Delaunay and Voronoi tesselations are assemblies of m such elementary cells, such that $\chi = \frac{\langle V \rangle - V_{min}}{m}$. The aggregate probability distribution function $f(V, m)$ reads:

$$f(V, m) = \frac{m^m}{(m-1)!} \frac{(V - V_{min})^{m-1}}{(\langle V \rangle - V_{min})^m} \exp\left(m \frac{V - V_{min}}{\langle V \rangle - V_{min}} \right). \tag{4.9}$$

This prediction has successfully been compared to free volume distributions that have been experimentally measured in monodisperse packings of frictional spheres in air and in solvent [99]. In these experiments the packing density has been varied been random loose packing (rlp) ($\phi \approx 0.55$) and random close packing (rcp) $\phi \approx 0.64$.

Experiment: Voronoi area distribution

For our two-dimensional foam system we will calculate the free *area* probability distribution $p(A)$. This procedure has been carried out for bidisperse two dimensional packings of hard discs by Lechenault et. al [102],

and for each species they observe a distribution similar to similar to Eq. (4.9) — here the discs are essentially undeformed and the density lies below random close packing. In contrast, we will investigate free area distributions in bi-disperse foams approaching ϕ_{rcp} ($= 0.842$ in foams) from the high density, jammed side. That is, we will extract $p(A)$ from the set of runs we have discussed before with ϕ varying between 0.855 and 0.975.

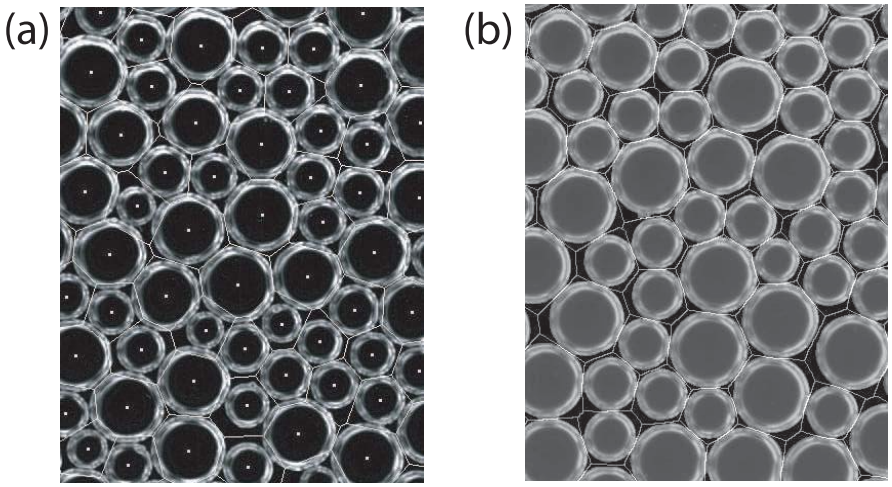

FIGURE 4.11: (a) Standard Voronoi tessellation of the bubble centers: For neighbours that differ in size Voronoi cell perimeters intersect bubbles. (b) The navigation map tessellation respects the bubble edges and follows the curvature of the contacts.

We measure the probability distribution of free areas $p(A)$ by calculating the Voronoi area distribution of the grid of points that represent the centers of mass of the bubbles. For a given grid of points, the Voronoi tessellation yields cells in which all points are closer to a certain grid point than to any other grid point [103]. The Voronoi cell perimeters are thus perpendicular bisections of the vectors connecting a grid point and its nearest neighbours, see Fig. 4.11(a). As a result, for a bidisperse packing, the Voronoi cell edges do in general not respect the bubble perimeter and thus the Voronoi cell does not represent the free area per bubble. For hard spherical objects one can get around this problem by weighting the grid points according to the sphere radius (Voronoi-Laguerre tessellation),

however, in our experiment, the bubbles are not only bidisperse, but in general also deformed and the flattened contacts can be curved.

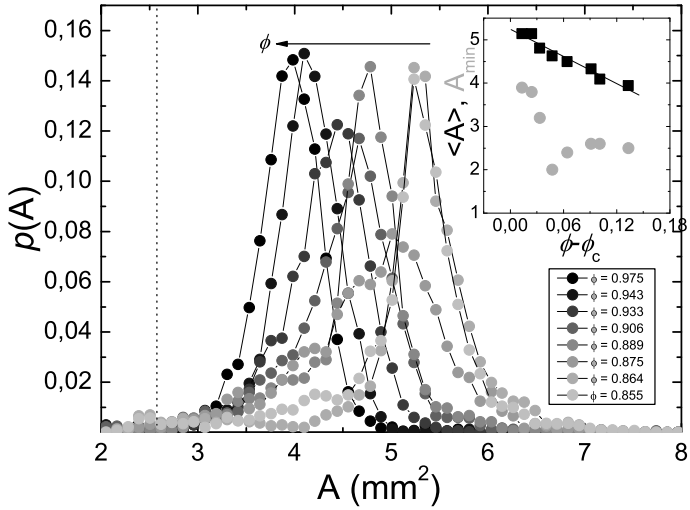

FIGURE 4.12: Distribution of Voronoi area for packings between $\phi = 0.875$ and $\phi = 0.975$. The average Voronoi area $\langle A \rangle$ (black squares) and A_{min} (red dots) are plotted as a function of ϕ in the inset. The vertical dashed line indicates the minimal free Voronoi area for the small bubbles at $\phi = 0.965$ which is given by $A_{min} = \frac{\pi}{4}(1.8)^2/0.965 = 2.63$ mm^2.

To fully take the effects of both deformations and bidispersity into account, we calculate what is called the navigation map [103, 104]. To this end, we take the Delaunay triangulation — which is the dual representation of the Voronoi tesselation — of the grid of bubble centers. Each triangle is divided in 4 areas: three areas each represent the part of a bubble that is inside the triangle and the fourth area corresponds to the interstice. We can illustrate this with a hexagonally ordered, monodisperse foam: in this case the Delaunay triangles connect three bubbles at angles of 60° and the interstice is exactly in the center of the triangle. For all pixels in the interstice we calculate whether they are closest to any point on the perimeter of one of the three bubble areas. The result is shown in Fig. 4.11(b): we obtain free areas per bubble that respect the bubble edges and follow the curvature of the contacts.

We calculate $p(A)$ from the experimental data at a gap width $W = 5$

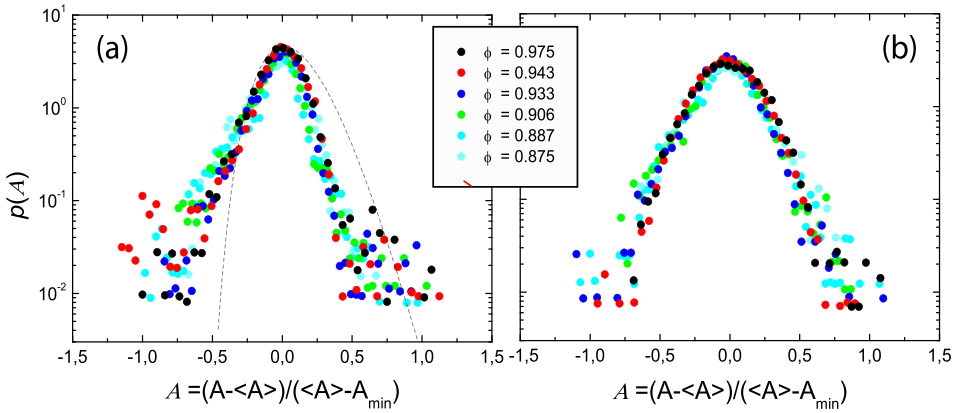

FIGURE 4.13: (a) Voronoi area distributions for small bubbles at various ϕ (see inset) centered around $\langle V \rangle$ and rescaled by the variance $\langle V \rangle - V_{min}$. Dashed line shows a solution to Eq. (4.9), highlighting the qualitative differences. (b) Voronoi area distributions for large bubbles centered around $\langle V \rangle$ and rescaled by the variance $\langle V \rangle - V_{min}$.

cm that also yielded ϕ and Z as well as the velocity profiles that were used to establish the scaling of k vs ϕ. We state the details: we have performed a scan over ϕ at fixed driving velocity $v_0 = 0.26$ mm/s. We have obtained 3000 images per packing fraction, and we calculate $p(A)$ over a central region of every 100th frame. We subsequently average the individual $p(A)$ distributions to improve statistics. We have measured $p(A)$ for $0.855 \leq \phi \leq 0.975$. We obtain bimodal distributions, which we can split according to the size of the bubbles inside the Voronoi areas. Distributions for the smaller bubbles are shown in Fig. 4.12: for increasing ϕ the average of the distribution shifts to smaller values (see black squares in inset of Fig. 4.12). From these distributions we can also extract A_{min} (red circles in inset of Fig. 4.12). We check that the value of A_{min} that we extract makes sense by calculating its value for $\phi = 0.965$ in the following way: from the size histograms presented in Chapter 2, we know that at that packing fraction, the average small bubble diameter equals 1.8 mm. The miminal free area for such a bubble (in a hexagonal packing of same sized bubbles) equals $A_{min} = \frac{\pi}{4}(1.8)^2/0.975 = 2.63$ mm^2, in good agreement with the value extracted at $\Delta\phi = 0.12$ (see inset of Fig. 4.12).

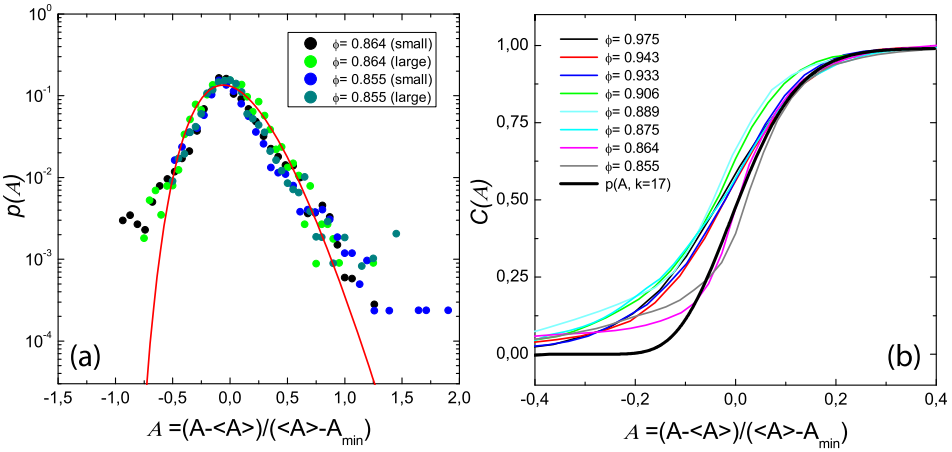

FIGURE 4.14: (a) Voronoi area distributions for small and large bubbles at $\phi = 0.864$ and $\phi = 0.855$ (see inset) centered around $\langle V \rangle$ and rescaled by the variance $\langle V \rangle - V_{min}$. Solid black line is solution to Astes prediction Eq. (4.9) with $m = 17$. (b) The cumulative sum $C(A)$ for all small bubble distributions evidences a sudden crossover to the Aste prediction: for the two lowest ϕ-values, $C(A)$ resembles the predicted $C(A, m = 17)$.

We rescale the distributions by $(A - \langle A \rangle)/(\langle A \rangle - A_{min})$ that is, we center the distributions around the average of the distribution and rescale the width by a free parameter $\langle A \rangle - A_{min}$ which is the variance of the distribution and which can be identified with the granular temperature χ. We plot all rescaled distributions, except those obtained for $\phi = 0.864$ and $\phi = 0.855$ in Fig. 4.13: the left figure (a) shows the collapse of Voronoi area distributions for the small bubbles and the right figure (b) shows the collapse for the large bubbles. Note that the collapse is optimized by variable values of A_{min} which are estimated from the unscaled distributions, see Fig. 4.12. The distribution of the small bubbles appears to be slightly skewed with exponential tails, while the distribution of the large bubbles appears to be symmetrical around $\langle A \rangle$. In this case it is hard to tell whether the tails are exponential or Gaussian. A striking result is thus that the distributions for small and large bubbles do not have the same shape. Furthermore, by comparing the distributions to the Aste prediction $f(V, m)$ were we replace V with A, see dashed line in Fig. 4.13(a)), we

see that both rescaled distributions have a markedly different shape than the analytical prediction.

The Voronoi area distributions of the runs that were performed closest to the jamming transition ($\phi = 0.864$ and $\phi = 0.855$) do not collapse on the master curves presented in Fig. 4.13. We instead plot the distributions for both the large bubbles and the small bubbles together in Fig. 4.14(a). We can observe a reasonable collapse and by overplotting the solution to Eq. (4.9) with $m = 17$ we see that close to ϕ_c the distributions appear to cross over to the shape predicted by this equation.

This is also evidenced in Fig. 4.14(b): here we plot the cumulative distribution $C(A)$ defined as:

$$C(A) \equiv \int_{A_{min}}^{A} p(A')dA'. \tag{4.10}$$

We compare the distibutions $C(A)$ for small bubbles, obtained at various ϕ, to the $C(A, m = 17)$ predicted by Aste et al. [99, 101] that we obtained by fitting to the data in Fig. 4.14(a). We see that the shape of $p(A)$ is the same for all runs except for the runs performed at $\phi = 0.864$ and $\phi = 0.855$. We further see that it quite suddenly crosses over to the shape predicted by Eq. (4.9) for these two runs closest to ϕ_c, indicating that one recovers the Aste prediction close to ϕ_c.

Discussion

We have thus seen that for densely packed two-dimensional foams the Voronoi area distributions $p(A)$ do not comply with the theoretical prediction by Aste et al., but that as one nears the unjamming density ϕ_c, the distributions do seem to cross over to this behaviour. This might be understood by considering the fact that the Aste distribution is well-defined and tested in hard granular materials at densities between ϕ_{rlp} and ϕ_{rcp} and for two-dimensional foams (and frictionless systems in general) $\phi_{rcp} = \phi_J$, such that we approach the region of densities in which Eq. (4.9) applies upon lowering the packing density of the foam.

Note however, that the value $m = 17$ that yields an acceptable agreement between $f(A, m)$ and $p(A)$ is remarkably high, when one interprets this value to be associated with the average number of nearby bubbles that border the free area per bubble, which is 6 for a two-dimensional packing.

4.3.2 The force distribution $p(f)$

In disordered systems the distribution of particle forces is often strongly heterogeneous. In granular systems in particular, forces are typically transmitted along force chains [15,105], which implies that part of the particles bear a very large load while another part hardly participates in transmitting forces. As a result, the distribution of contact forces $p(f)$ in such systems is generally broad, with frequent occurrence of very large inter-particle forces.

Both theoretical and experimental investigations ([106] and references therein) generally yield force distributions that exhibit a peak around the average force in the system and a broad tail that is either exponential or Gaussian. In a recent Letter, [106], Tighe and coworkers show that if the proper constraints are taken into account, a Gaussian tail emerges, and it should be noted that the limited statistics available to experimentalists often impede a clear-cut distinction between a Gaussian or an exponential tail. O'Hern et al. [6] also argue that the way one averages over force distributions obtained from distinct packings influences the observed shape of the tail. In the same paper, these authors also identify the appearance of a peak in the force distribution with jamming, implying that for unjammed systems $p(f)$ decreases monotonously.

Extracting $p(f)$ from experimental images

We obtain $p(f)$'s for foams at varying ϕ from the navigation map Voronoi tessellations discussed in the preceding section. Since the tiles in this tessellation respect the bubble edges and follow their curvature, we can overlay the Voronoi cell edges with the images that have yielded ϕ, see Fig. 4.2. In this way we can extract the size of the deformed contacts between touching bubbles i and j which is $2\kappa_c$, as can be seen in Fig. 4.15. This contact size is related to the elastic force f_{ij} through the relation Eq. (1.7):

$$f_{ij} = f_i + f_j = \pi\kappa_c^2 2\sigma \frac{R_i + R_j}{R_i R_j}, \tag{4.11}$$

with κ_c the radius of the deformed contact and $R_{i,j}$ the radii of bubbles i and j respectively. Note that this relation is valid when deformations are small. Whether it breaks down for larger deformation we do not know, but simulations by Lacasse et al. [17] on the interaction law in three-

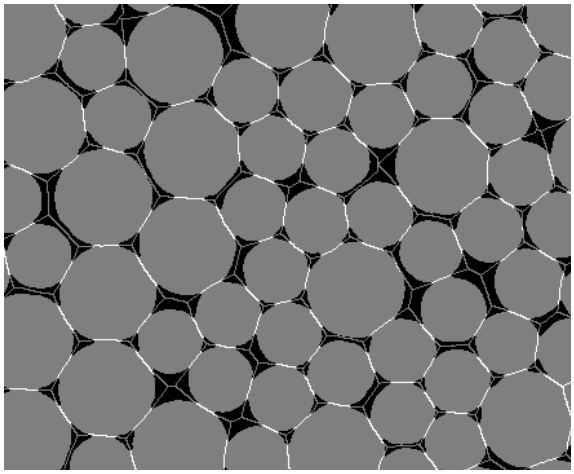

FIGURE 4.15: Illustration of the procedure used to extract $p(f)$: the Voronoi cell boundaries are plotted together with the ϕ plots. Where bubbles overlap, the cell boundaries are bright. The size of this contact is proportional to $\sqrt{f_{ij}}$.

dimensional emulsions provide good hopes that we can assume an interaction like Eq. (4.11) to hold for our two-dimensional foam. Note that since $\kappa_c^2 \propto \xi$ with ξ the overlap, this is the linear harmonic interaction we discussed before.

We use the same experimental images as in the previous section, and hence obtain force distributions at 8 different values of ϕ. For each ϕ we compute $p(f)$ over 30 frames. In Fig. 4.16 we show the normalised distributions for each ϕ. As ϕ decreases towards ϕ_c, we see the peak in $p(f)$ move towards $F = 0$, in accordance with the conjecture that the disappearance of the peak in $p(f)$ signals the jamming transition.

We cannot clearly distinguish the shape of the tails of $p(f)$ over more than two decades, be we do observe a trend in that the distributions seem to exhibit exponential tails near jamming, but become more and more Gaussian the more compressed the system becomes.

Averaging over distinct packings

Note that we have computed the averaged $p(f)$ by simply summing the distributions for each frame. In [98] O'Hern and coworkers argue that

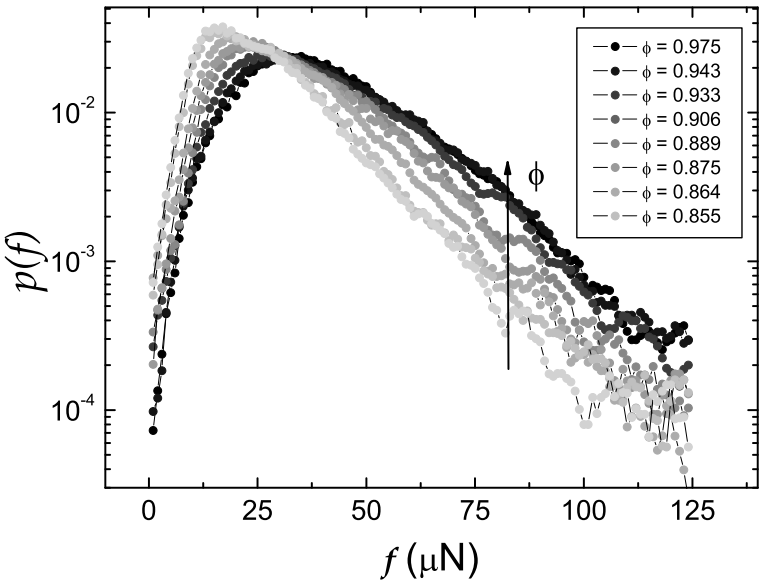

FIGURE 4.16: Force distribution functions obtained by averaging those of 30 different realisations. For decreasing ϕ the peak moves towards $f = 0$ and the shape of the tails appears to cross over from Gaussian to exponential.

the way one calculates the average force distribution from a set of distributions obtained for distinct particle configurations greatly influences the shape of the tails. These authors show that if one simply takes the histogram of all forces from all configurations and then normalises the forces by the force $\langle\langle f\rangle\rangle$ which is the average over all these forces, exponential tails will be seen. Note that this is not the same as the procedure we have followed to calculate the $p(f)$'s in Fig. 4.16. The alternative procedure that is analysed in [98] is to normalise the forces for each packing by their average $\langle f\rangle$ and then perform the summation, in which case one will observe Gaussian tails.

We plot force distributions for different ϕ obtained in the latter way in Fig. 4.17. We do not see a qualitative difference in the trend that the shape of the tails follow between Fig. 4.16 and Fig. 4.17. We do, however, see that the relative contribution of the large forces grows for packings which are closer to ϕ_c in accordance with [6, 16, 98].

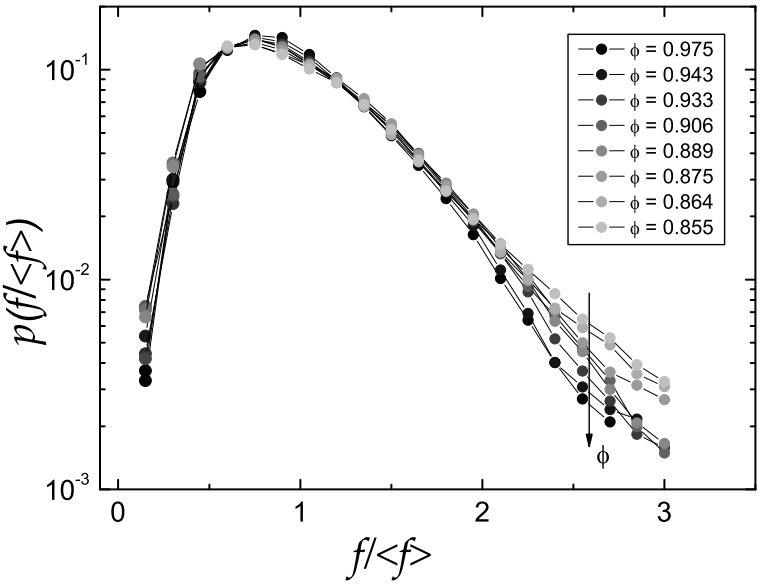

FIGURE 4.17: Force distribution functions obtained by averaging those of 30 different realisations that have each been rescaled by their average force $\langle f \rangle$. For decreasing ϕ the relative contribution of large forces increases and the shape of the tails appears to cross over from Gaussian to exponential.

Discussion

We have performed highly exploratory measurements on the shape of the force distribution $p(f)$ as a function of the distance to jamming. Despite limited statistics, we see globally the same trends as previous authors, e.g., the cross-over from Gaussian to exponential tails and a broadening of the distribution upon approaching ϕ_c. A signature of the precision with which we can measure is to check whether the forces on each bubble are in balance. We find that the error in the force balance per bubble is typically 30% of the sum of all forces on the bubble, which is rather high. This might be due to the fact that slight displacements of the Voronoi cell edges with respect to the bubbles results in a large overestimation of the contact forces due to the circular shape of the bubbles. Also note that the images we analyse are from a sheared foam which means that force balance is not necessarily satisfied. The strong shearbanding in the system, how-

ever, means that the region of interest is hardly flowing, implying that the system is at least close to force balance.

4.3.3 The shear modulus G

The nature of the phase boundaries separating the jammed and the flowing phase is one of the more crucial questions the jamming phase diagram has generated. The simulations [6, 80] have focused on the transition at point "J" (see Fig. 4.10), located at ϕ_c on the density axis, and have evidenced surprising behaviour at this point: the average number of contacts between particles jumps abruptly while the bulk and shear elastic moduli B and G vanish smoothly with critical exponents. Surprisingly, the elastic moduli scale differently: B scales as $(\phi - \phi_c)^{\alpha-2}$, while G scales as $((\phi - \phi_c)^{\alpha-3/2}$, where the exponent α depends on the interaction potential between particles. Irrespective of this interaction potential, the ratio G/K scales as $Z - Z_c$. As a result, jammed systems become much softer to a shear deformation than to a compression, the closer they are to ϕ_c . Furthermore, a length scale ξ related to correlated, vortical motions of the particles, is expected to diverge [6, 80].

In this section, we propose experiments on two-dimensional foams to establish the critical scaling of B and G with $\Delta\phi \equiv \phi - \phi_c$. We will show preliminary data on the shear modulus G to show this techniques' tremendous promise.

We measure the mechanical response of foams at point J in the following way: we trap a monolayer of bubbles in a Taylor-Couette geometry, consisting of two concentric cylinders, see Fig. 4.18(a). We further cover the bubbles with a glass plate, to precisely vary ϕ. The foam is driven by the Anton Paar DSR-301 rheometer which can measure and exert the extremely small stresses and rotations associated with the regime in which foams responds elastically. By using a grooved inner cylinder we shear the foam and hence measure G, see Fig. 4.18(a(i)) while by attaching a different and novel geometry, we will measure the response under compression and hence B, see Fig. 4.18(a(ii)).

The bubbles experience additional viscous drags with the glass plates, but we apply very small step strains (γ= 0.01 %) with the rheometer and only measure the stress after the viscous stresses have relaxed and the resulting signal reflects the elastic response (see Fig. 4.18(b)). One can easily extract the elastic moduli from this signal and by repeating the measure-

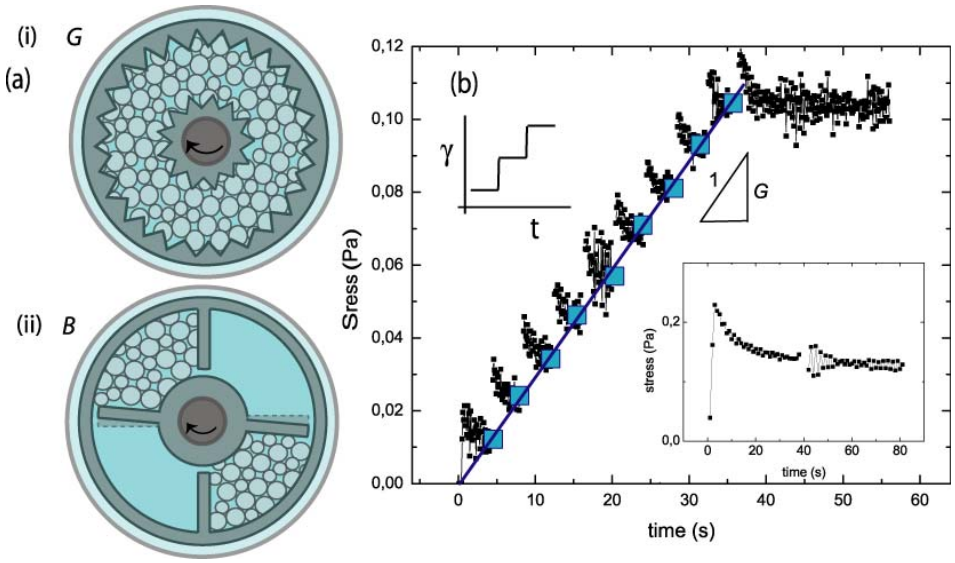

FIGURE 4.18: Schematic picture of the proposed experiments: a monolayer of foam bubbles is loaded in a Couette geometry with top plate and step strains are exerted by the inner cylinder, which is connected to a rheometer head: (i) setup to measure shear modulus G. (ii) setup to measure bulk modulus B. (b) Preliminary measurements of the shear response of a twodimensional foam to step strains: After a viscous transient (see inset), the stress signal reflects only the elastic stress and the slope of the straight line is the shear modulus G.

ments at varying packing fractions and different geometries we can establish the scaling of G and B with ϕ. By looking at the elastic response of the foam to deformations we stay inside the jammed region of the jamming phase diagram at all times and essentially measure along the zero stress, zero temperature axis, see Fig. 4.10.

In Fig. 4.19 we plot the measured stress as a function of time, while applying a small step strain every 4 seconds. We clearly see the viscous transient and the subsequent elastic signal, and while have not been able to exactly measure the density ϕ we have monotonously increased the gap between the fluid and the glass plate and thus we have monotonously increased ϕ. Fig. 4.19 shows the response of the foam at varying ϕ: the shear modulus G increases monotonically with ϕ. Clearly these measurements have to be expanded and performed in a quantitative manner to establish

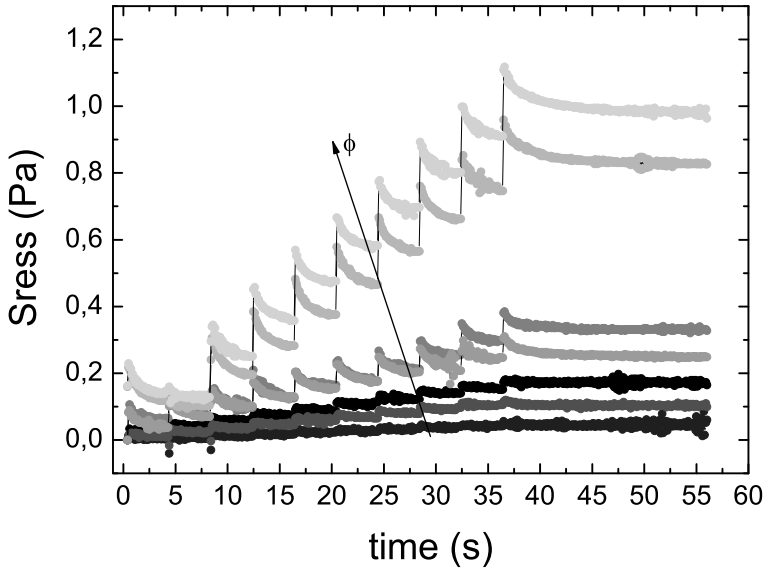

FIGURE 4.19: (a) A monolayer of foam bubbles is loaded in a Couette geometry and step strains are exerted by the inner cylinder, which is connected to a rheometer head, at varying ϕ denoted by arrow. The shear response of a two dimensional foam to step strains becomes increasingly strong and hence G increases when ϕ increases.

critical scaling of the shear modulus G, but nevertheless, these preliminary runs show the huge potential of confined foams to investigate the linear response of soft disc systems near jamming.

4.4 Conclusion

In this chapter, we have discussed a multitude of phenomena that strongly depend on the density ϕ of sheared or static two-dimensional foams. In particular, we have for the first time experimentally established scaling of the inverse foam consistency k and the contact number Z with $\Delta\phi$, and we have observed the predicted shift towards zero of the peak of $p(f)$ as we approached ϕ_c. Also, we have obtained the first indications that G indeed vanishes at point J, even though we cannot establish the scaling yet. In contrast, we have observed peculiar distributions of the Voronoi

area distributions that appeared to be independent of ϕ, except close to the transition, where a sudden crossover towards the prediction for a hard-sphere systems was observed.

Clearly these findings open all sorts of exciting inroads into the behaviour of foams as a function of the bubble density, and many could be put on a firm footing with simply more statistics and a closer approach of ϕ_c.